ANALYSIS OF FLUID FLOW IMPACT OSCILLATORY PRESSURES WITH AIR ENTRAPMENT AT STRUCTURES

Robert Mayon[1]* Zoheir Sabeur[2] Mingyi Tan[3] and Kamal Djidjeli[4]

Hydrodynamic wave loading at coastal structures is a complex phenomenon to quantify. The chaotic nature of the fluid flow field as waves break against such structures has presented many challenges to Scientists and Engineers for the design of coastal defences. The provision of installations such as breakwaters to resist wave loading and protect coastal areas has evolved predominantly through empirical and experimental observations. This is due to the challenging understanding and quantification of wave impact energy transfer processes with air entrainment at these structures. This paper presents a numerical investigation on wave loading at porous formations including the effects of air entrapment. Porous morphologies generated from cubic packed spheres with varying characteristics representing a breakwater structure are incorporated into the numerical model at the impact interface and the effect on the pressure field is investigated as the wave breaks. We focus on analysing the impulse impact pressure as a surging flow front impacts a porous wall. Thereafter we investigate the multi-modal oscillatory wave impact pressure signals which result from a transient plunging breaker wave impinging upon a modelled porous coastal protective structure. The high frequency oscillatory pressure effects resulting from air entrapment are clearly observed in the simulations. A frequency domain analysis of the impact pressure responses is undertaken. We show that the structural morphology of the porous assembly influences the pressure response signal recorded during the impact event. The findings provide good confidence on the robustness of our numerical model particularly for investigating the air bubbles formation and their mechanics at impact with porous walls.

Keywords: Porous structures; fluid structure interaction; compressible flow; OpenFOAM

INTRODUCTION

Severe damage can be inflicted on coastal defence structures as a result of high intensity wave forces. Laboratory experiments have previously been performed to gain an understanding of the physical processes which occur at the wave impact interface e.g. (Topliss et al., 1993), (Bullock et al., 2006), (Bullock et al., 2007), (Bredmose et al., 2009). However the validation of these wave impact pressure response results has proven to be very difficult because of the highly nonlinear, transient nature of the wave breaking process (Chan and Melville, 1988).

The progressive damage sustained by coastal defences may be attributed to their continuous exposure to transient wave impact pressures. At the present time these forces are not fully understood and the long term durability of coastal defences is difficult to determine (Oumeraci et al., 1993), (Wemmenhove et al., 2015), (Alagan Chella et al., 2015). In addition to these short duration impulse impact pressures, resonant oscillatory pressure signals have been observed in many experimental studies (Bagnold, 1939), (Hattori et al., 1994), (Sabeur et al., 1998), (Peregrine, 2003), (Stagonas et al., 2016). These oscillations manifest themselves subsequent to the initial wave impact with solid or porous walls and may be a source of much damage and deterioration to the structural integrity of coastal defences. Researchers have speculated as to the source of the observed oscillations within the pressure response signal (Peregrine, 2003).

Experimental work has shown that incident waves on vertical structures can produce impulse pressures which greatly exceed magnitudes of the typical pressures that are expected when employing shallow water wave theory methods for analysis (Peregrine, 2003). The magnitude of these impulse pressures can commonly exceed:

$$10\rho g(h + H) \qquad (1)$$

Where H is the wave height, h is the water depth, ρ the water density and g the acceleration due to gravity. These higher magnitude impulse pressures have been attributed to a phenomenon often termed as the wave 'flip-through' effect, (Peregrine, 2003). However, additional highly destructive oscillatory pressure effects have been observed in experimental studies, most noticeably when air bubbles are

[1] Southampton Marine and Maritime Institute, University of Southampton, UK
[2] IT Innovation Centre, Department of Electronics and Computer Science, University of Southampton, UK
[3] Fluid Structure Interaction Group, Faculty of Engineering and Environment , University of Southampton, UK
[4] Computational Engineering and Design Group, Faculty of Engineering and Environment, University of Southampton, UK
*Corresponding Author

entrained at impact. In this instance, the entrapped air bubbles will compress and dilate with a range of specific oscillatory frequencies. Further, and according to earlier theoretical, (Minnaert, 1933) and experimental studies, (Hattori et al., 1994), the frequency range with which these bubbles oscillate will be dependent on the size of the entrained air void during their formation. The authors of this study have also observed these effects in previous numerical simulations, see e.g. (Mayon et al., 2016).

In this work we analyse the impact of a solitary wave with a porous interface while employing a CFD approach. First we briefly introduce the theory for modelling free surface fluid flow; and the numerical methods to simulate wave impact at porous structures. We also introduce theories and experiments from the literature which show the relationships between formed sizes of air bubbles in fluid flows and their typical resonance frequencies of oscillation. We investigate 3 dimensional numerical dam-break flow simulations with impact at varying morphology porous vertical wall interfaces. The numerical model is capable of capturing the compressible effects of the air phase during bubble formation.

FREE SURFACE FLOW AND BUBBLE OSCILLATION THEORIES

Numerical Methods

The numerical simulations were preformed using the finite volume technique based open source CFD code OpenFOAM, (The openFOAM Foundation, 2013). This software is compiled as a collection of C++ libraries with dedicated pre-programmed solvers which can be used to model various fluid flow simulation scenarios. In this study, the compressibleInterFoam solver was used to examine the effects of air entrapment in the fluid phase during wave breaking. This solver uses the phase fraction based Volume of Fluid method (VOF), (Hirt and Nichols, 1981), to capture and represent the interface between the two fluids.

Volume of fluid method

The interaction of the individual fluid phase constituents in the model is important as the pressure transfer across the free surface boundary which defines an entrained air bubble is central to this study. In the volume of fluid method a function, $\alpha(x, y, t)$, is introduced at each grid cell in the model domain. The value of this function is defined as unity at any cell which is fully occupied by the fluid; and zero at any cell completely devoid of fluid. Cells with intermediate values may contain a droplet, a bubble or are located such that the interface between the two fluids intersects that cell. In the VOF method, the temporal evolution of the phase fraction function and thus the advection of the flow in two dimensional space is governed by the following transport equation:

$$\frac{\partial \alpha}{\partial t} + u\frac{\partial \alpha}{\partial x} + v\frac{\partial \alpha}{\partial y} = 0 \tag{2}$$

Where the phase volume fraction $\alpha \in [0, 1]$, and u and v are the fluid velocities in the x and y direction respectively. By calculating the derivatives of the α function at each cell boundary the free surface normal can be established, (Sabeur et al., 1995). The normal direction to the free surface is then the direction in which the α function varies most rapidly (i.e.$\nabla\alpha$). From the value of the α function and the direction of the normal to the fluid interface, a line cutting the cell can be drawn which represents the free surface boundary.

Compressible model governing equations

The conservation of mass equation for an incompressible fluid is defined as follows:

$$\nabla \cdot \boldsymbol{U} = 0 \tag{3}$$

Using Equation (3) the two phase conservation of mass equation for the volume fraction $\alpha \in [0, 1]$ can be represented as:

$$\frac{\partial \alpha}{\partial t} + \nabla \cdot \boldsymbol{U}\alpha + \nabla \cdot [\boldsymbol{U}_c \alpha(1-\alpha)] = 0 \tag{4}$$

Where $\boldsymbol{U}$ is the fluid velocity vector, and $\boldsymbol{U}_c$ is the artificial compression velocity vector given by $\boldsymbol{U}_c = \boldsymbol{U}\alpha_1 - \boldsymbol{U}\alpha_2$. The final term on the left hand side ensures a sharp interface is maintained between the fluid phases (Berberović et al., 2009). The momentum conservation equation is formulated by summing the averaged fluid properties according to their constituent proportion in the boundary cell. For a two phase flow, density ρ in the cells is given by:

$$\rho = \sum_{\alpha=1}^{2} r_\alpha \rho_\alpha \tag{5}$$

Where r_α is the volumetric fraction of each constituent fluid in the free surface boundary cell. A single momentum conservation equation for an incompressible fluid can then be defined for the homogeneous mixture as:

$$\frac{\partial(\rho \boldsymbol{U})}{\partial t} + \nabla \cdot (\rho \boldsymbol{U}\boldsymbol{U}) = -\nabla p_h + \nabla \cdot \mu(\nabla \boldsymbol{U} + \nabla \boldsymbol{U}^T) + \boldsymbol{F}_s + \rho \boldsymbol{f}_i \tag{6}$$

Where ρ is given in Equation (5), p_h is the hydrostatic pressure, μ is the fluid viscosity and $\boldsymbol{f}_i$ is the gravitational force. The term $\boldsymbol{F}_s$ represents the surface tension force and is calculated from $\boldsymbol{F}_s = \sigma\kappa\nabla\alpha$, where σ is the interfacial tension and the interface curvature is given by $\kappa = \nabla\cdot(\nabla\alpha/|\nabla\alpha|)$.

To include the effects of compressibility within the model an Equation of State (EOS) must be defined for each phase. For the air phase, the ideal gas EOS is specified as follows:

$$\rho_a = p\frac{1}{R_a T} \tag{7}$$

Where ρ_a is the air density, R_a is the specific gas constant for air, T is the air temperature and p is the pressure. For the water phase the perfect fluid EOS is defined as:

$$\rho_w = p\frac{1}{R_W T} + \rho_{W0} \tag{8}$$

Where ρ_{W0} represents the density of water at atmospheric pressure conditions. To allow for air to be modelled as a compressible medium an additional term must be incorporated into Equation (4):

$$\frac{\partial \alpha}{\partial t} + \nabla \cdot \boldsymbol{U}\alpha + \nabla \cdot \boldsymbol{U}_c\alpha(1-\alpha) = -\frac{\alpha}{\rho_W}\frac{D\rho_W}{Dt} \tag{9}$$

The Euler compressible mass conservation equation is defined as:

$$\frac{\partial \rho}{\partial t} + \nabla \cdot (\rho \boldsymbol{U}) = 0 \tag{10}$$

The transport equation for the temperature term is derived from the energy conservation equation, (Martínez Ferrer et al., 2016), and is calculated accordingly using equation (11) below:

$$\frac{\partial \rho T}{\partial t} + \nabla \cdot (\rho \boldsymbol{U} T) - \Delta(\mu T) = -\left(\frac{\alpha}{C_W} + \frac{1-\alpha}{C_a}\right)\left(\frac{\partial \rho k}{\partial t} + \nabla \cdot (\rho \boldsymbol{U} k) + \nabla.(\boldsymbol{U} p)\right) \tag{11}$$

C_W and C_a are the specific heat capacities for water and air respectively, while k is the specific kinetic energy. A flow field solution can be obtained by applying the PIMPLE algorithm which is a pressure-velocity coupling approach derived through combining the PISO and SIMPLE algorithms.

Resonant oscillation Frequency of a single entrained air bubble

The behaviour of a single air bubble which is entrained within an infinite water domain has previously been studied by Minnaert (1933). An analytic expression describing the resonant frequency of a spherical bubble which is subjected to an external impulse force is given by:

$$f = \frac{1}{2\pi r}\sqrt{\left(\frac{3\gamma p}{\rho}\right)} \tag{12}$$

Where r is the bubble radius, γ is the polytrophic coefficient of the fluid, p is the hydrostatic pressure at the depth which the bubble is located in the liquid and ρ is the liquid density.

Hattori et al. (1994), have conducted experiments to investigate the influence of air entrainment on impact pressures from a wave impinging on a vertical solid wall. By varying the wall location relative to the breaking wave they were able to capture and analyse the effects of 4 distinct geometries of the breaking wave. High speed video recording at the impact interface was captured, from which still images were provided. From their experimental analysis the oscillating frequency of an entrained bubble is given by:

$$f_{ap} = 180(2r)^{-0.5} \quad (13)$$

3 DIMENSIONAL POROUS IMPACT INTERFACE SIMULATION

There are two main approaches to modelling fluid transport in porous media. The first approach is the macroscopic continuum method wherein the flow is modelled according to the Navier-Stokes equations with an additional Darcy (or Darcy-Forcheimer) term incorporated into the momentum equation in the region where the porous structure is located (Higuera et al., 2014). In this method the physics of the flow through the porous medium is governed by phase quantities averaged over control volumes (also known as Representative Elementary Volumes).

The second approach to modelling fluid flow through porous media is a direct modelling approach wherein each phases is explicitly represented and the flow through the porous interstices is modelled explicitly using the Navier-Stokes equations. Other methods for modelling flow in porous media include the smoothed particle hydrodynamic (SPH) method and lattice Boltzmann methods. In this study the direct modelling approach is employed.

For this investigation a number of porous geometries were generated and incorporated into the OpenFOAM CFD model. Various parameters were used to classify the porous structure according to its morphology. These parameters include porosity, specific surface area, tortuosity and permeability.

Porous structure classification

Porosity

A porous sample in in its most basic definition is a material composed of a certain solid volume which contains a proportion of distributed void space. These voids can be occupied by one or more fluids in either a liquid phase, a gaseous phase or both. Thus porosity or the purpose of this investigation is defined as the fraction of the bulk volume of the sample which is occupied by pore or void space. Civan (2011) provides a mathematical definition of porosity as:

$$\Phi = \frac{\sum_{j \neq s} \Delta V_j}{\Delta V_b} \quad (14)$$

Where ΔV_b is the bulk volume of the porous sample or the total volume occupied by all phases, ΔV_j is the volume occupied by the jth phase and s denotes the sum of the solid phases forming the porous matrix.

Bear (1988) provides a more onerous characterisation of a porous media which suggests that the multiphase matrix must satisfy certain conditions such as level of void space interconnectedness, lower bound limits on interstitial surface areas and uniformity in phase distribution. However the definition of a porous medium is still couched in ambiguity as there is no complete consensus on limits for any of the above conditions.

Specific surface area

The specific surface area of a porous sample is defined as the interstitial void (or solid) surface area per unit bulk volume having a reciprocal length dimension. In molecular science specific surface area greatly influences adsorption rates and reactivity processes. However on a macroscale scale it can also be used to characterise the morphology of the porous structure. A higher specific surface implies a more complex porous media. Additionally a high specific surface area may also decelerate the flow of fluid through the porous structure as the wall shear stress will have a more pronounced effect due to a higher phase interfacial area.

Tortuosity

Tortuosity is an inherent characteristic of a porous media morphology which in general terms can be described as a ratio of the distance traversed by a fluid element between two fixed points to the straight line distance between those two points as shown in Figure 1(Brus et al., 2014). Tortuosity can be calculated from:

$$\tau = \frac{L_e}{L_s} \geq 1 \quad (15)$$

Where L_s and L_e are shown on Figure 1.

Whilst there has been a large body of academic research presented on the subject of tortuosity, there is no general agreement for a single precise definition of tortuosity and to date a number of different measurements of tortuosity have been advanced for different applications. For example Ghanbarian et

al. (2013) in their review paper describe geometric tortuosity, hydraulic tortuosity, electrical tortuosity and diffusive tortuosity.

The difficulty in achieving a unanimous characterisation for tortuosity may be twofold; with the exception of very few materials, e.g. metals, dense rocks and some plastics (Dullien, 1992), most material exhibit porous behaviour to varying degrees at multiscale levels from microscopic through to macroscopic scale. The parameters which govern the tortuosity may vary dramatically within a single material at different scale lengths thus effecting the observed tortuous transport path length. Therefore depending on which scale of analysis is being considered, different fluid behavioural effects may dominate the calculated tortuosity ratio.

When analysing the flow of fluid through porous media either the geometric or hydraulic tortuosity is usually considered. Figure 2, Ghanbarian et al. (2013) presents a comparison of a hydraulic tortuous flow path and a geometric tortuous flow path. At the microscale multiphase interfacial parameters such as capillary pressures, surface tension effects and wall friction may all significantly influence the flow rate through a porous structure, however at larger scale lengths these effects may not warrant consideration due to the bulk of the flow being conveyed through larger fissures where wall friction, capillary and free surface effects are not the limiting constraints on the flow rate. Then, it may be more appropriate to use hydraulic tortuosity for microscale analyses and geometrical tortuosity at larger scales

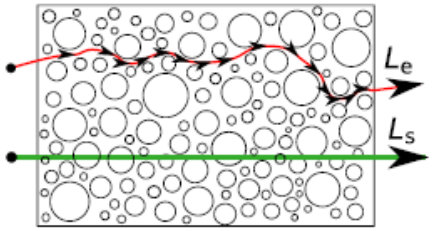

Figure 1 Tortuosity (Brus et al., 2014)

The structure of porous materials can take many forms, and the tortuous paths can vary from being comparatively simple to being highly complicated. For instance the porous structure of a natural material such as wood can be somewhat homogenous and anisotropic and thus in this case the tortuosity can be relatively simply described by reducing it to a model consisting of a bundle of unidirectional capillary tubes. This limiting case of a bundle of parallel, non-interconnected tubes longitudinally orientated in the direction of macroscopic flow, traversing the full thickness, L_s, of the sample presents little resistance to the flow (neglecting frictional effects at the tube wall). Then, a flow streamline, L_e, tracing the path of the fluid will have a length similar to the thickness of the sample, i.e. the tortuosity factor can be calculated for Equation 15 and will have a value of unity.

In contrast a material may be much more complex and disordered having multidirectional interweaving fibrous filaments as evidenced within some filter materials or in paper products. Then, the structural morphology is much more difficult to define and the parameters which can be used to describe the tortuous nature of interconnecting porous voids can be very difficult to determine from the physical sample. In this study the void throats between the solid particles are relatively narrow such that the flow streamlines are seen to be influenced by the surface of the solid phase material in the CFD model. The hydraulic tortuosity is therefore adopted in this investigation.

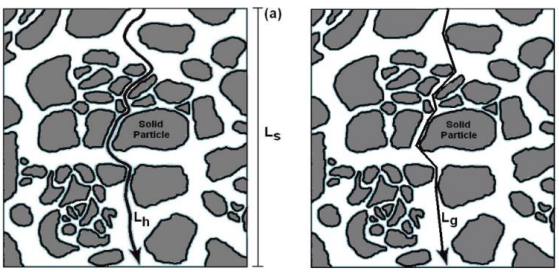

a. Hydraulic tortuous path **b. Geometric tortuous path**

Figure 2 Comparison between hydraulic tortuosity and geometric tortuosity, Ghanbarian et al. (2013)

Fluid flow through a porous medium is influenced by both the amount and morphology of the void (pore) space (Vallabh et al., 2010). While the amount of void space is easily quantified by measurement of porosity, the characterisation of the distribution of the void space structure is often very difficult, especially in complex, irregular porous media (Vallabh et al., 2010). In the case whereby the pore structure is more intricate with many converging and diverging channels the streamline path may not

follow the liner shortest distance between the bounding surfaces of the sample. Rather, the streamlines may be forced to follow a sinuous winding path determined by the morphology of the solid (or void) phase. Then the tortuosity factor must be greater than unity. This increases the time taken for the fluid to permeate through the porous media and results in an associated higher resistance to the flow. This is manifest in a lower permeability value for the sample. As the value of tortuosity approaches infinity this represents an internal pore structure (and geometric morphology) of increasing complexity. Furthermore, a thorough analysis and understanding of tortuous paths within a sample presents one with a means to quantify the complexity and also the permeability of the sample.

Simulated porous structure morphology

In an earlier study a thorough analysis of wave impacts with a solid interface were performed. A range of equation discretisation schemes were employed and the oscillatory behaviour of the resultant bubble(s) were analysed in depth, (Mayon et al., 2016).

In this study wave impact at a single porous morphology with varying component sphere sizes are investigated. The geometry consists of a number of spheres on a regular cubic lattice layout. The porous structures were generated using a short LISP file and the CAD software package AutoCAD Mechanical. The geometries were then exported as stereolithographic files. The OpenFOAM mesh generation utility snappyHexMesh was then used to construct an accurate 3-dimensional split-hex mesh which defined the void geometry within the porous structure.

In order to establish the exclusive influence of the various porous morphology characteristics; surface area, porosity, tortuosity, permeability, etc. on the wave impact pressure signal a range of simulations were conducted whilst varying the component sphere size. Each of these porous structures have mono-sized spheres arranged on a distinct regular geometric lattices. This work presented in this study will be restricted a single regular lattice layout; simple cubic packing. The following subsections describe the porous structure and how they are generated.

Simple cubic packing

This spherical based structure consists of a mono-sized, close packed sphere-swarm arranged on a cubic lattice layout. With the exception of the outermost spheres on the boundary of the lattice (and assuming that there is a minimum of 27 spheres composing the structure), each sphere is in direct contact with its 6 neighbours, this is also termed the coordination number. This sphere packing arrangement is also known as simple close cubic packing (see Figure 3).

Assuming the bounding box enclosing the lattice structure maintains a fixed volume and the spheres are tightly packed, then the porosity of the assembly is constant for any range of component sphere size. Thus due to the regular composition of the structure the porosity is maintained with a value of 0.476 for all simulations with the elemental spheres in a simple cubic packing system. The constant porosity is obvious from Figure 3. This allows one to investigate the influence of porous matrix component grain size on the flow field while maintaining the structure's overall density at a constant value. In this study a bounding cube of 100mm length was defined and 4 geometries based on packed sphere sizes of 25mm diameter, 12.5mm diameter, 6.25mm diameter and 3.125mm diameter were investigated.

Furthermore, the theoretical geometric tortuosity of the matrix which is an inherent characteristic of the porous structure and is determined by its geometrical composition also retains a constant value and is calculated according to Equation 15.

However if hydraulic tortuosity is employed then it can be easily shown mathematically that the tortuosity parallel to the flow direction varies from a minimum value of $\tau = 1.0$ to a maximum value of tortuosity $\tau = 1.57$ (irrespective of the elemental sphere diameter), assuming the flow streamline remains within the x-y plane of the fluid flow direction and is coincident with the sphere surfaces. The value of $\tau = 1.0$ is obtained if one considers a streamline which is located at maximum distance from the surface of the spheres, and $\tau = 1.57$ is obtained for a streamline which follows the contour of the spheres surface and assuming the streamline stays in the x-y plane (see Figure 3).

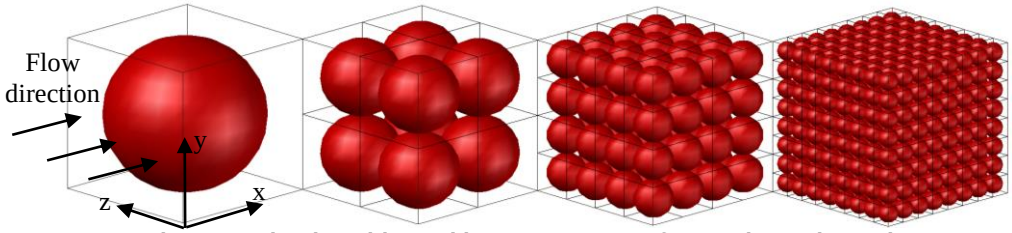

Figure 3: Simple cubic packing arrangement for varying sphere sizes

Table 1. Simple cubic packing structure characteristics*								
Sphere diameter	25mm		12.5 mm		6.25 mm		3.125 mm	
Porosity	47.64 %		47.64 %		47.64 %		47.64 %	
# of spheres	64		512		4,096		32,768	
Surface area	125,662mm^2		251,279mm^2		502,558mm^2		1,005,116mm^2	
Specific surface area	0.1257 mm^{-1}		0.2513 mm^{-1}		0.5026 mm^{-1}		1.0051 mm^{-1}	
Coordination number	6		6		6		6	
In-plane (analytic) Tortuosity	**min**	**max**	**min**	**max**	**min**	**max**	**min**	**max**
	1	1.57	1	1.57	1	1.57	1	1.57

*values calculated assuming spheres packed into cube of side 100mm

SIMULATION SETUP

The simulation set-up follows an earlier study presented in Mayon et al. (2016). Model verification and validation data may also be found in Mayon et al. (2016). The geometry is in the configuration of a dam break flow test case as shown on Figure 4 below. The numerical wave tank is 0.4m long and 0.2m high and 0.05m deep. The tank contains a column of water of width 0.05715m, height 0.01143m and depth 0.05m at the left hand side. A no-slip boundary condition is prescribed at the tank base and at vertical walls at x = 0, z = 0 and z = 0.05. As the top of the tank is considered to be open to the atmosphere, the inflow and outflow of fluid is permitted across this boundary. Thus, at this surface a combination of boundary conditions are specified for the pressure and velocity terms of the fluid flow governing equations to model inflow and outflow behaviour whilst maintaining the PIMPLE algorithm stability. The numerical value of the `fixedValue` boundary condition is set to atmospheric pressure conditions (101 kPa) across the surface which represents the top of the numerical tank. The porous morphologies were incorporated into the model at the right hand side of the domain. Additionally at the right hand side surface (at x = 0.4) the boundary condition applied permits the outflow of fluid from the domain. The pressure signals are sampled at mid height the face of the bottom sphere forming the porous matrix indicated by point P1 on Figure 4 below.

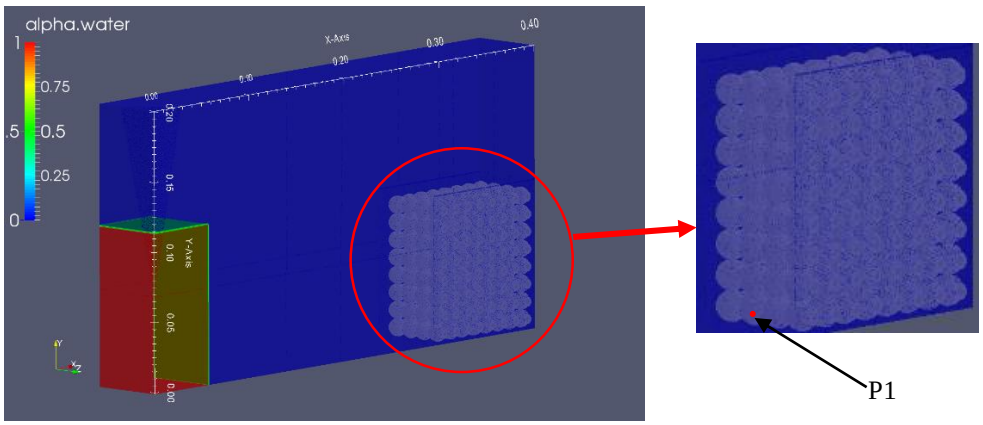

Figure 4: Section through simulation setup (sphere diameter 12.5mm)

As the flow simulation progresses, the water column collapses and the flow front advances towards the right hand side (RHS) of the numerical tank. The surging flow front impacts the porous structure and is forced vertically upwards through the formation of a thin jet. Figure 5 (a) presents the α function as the flow front impacts the wall. This initial impact produces the first pressure peak shown on Figure 7 at time t = 0.208. As the vertical jet collapses (Figure 5(c)) it forms a plunging breaker type wave and converges with the fluid below, a bubble is entrained in the flow. For the 3.125mm diameter cubic packed sphere structure this occurs at t = 0.515 seconds (Figure 5(d)) and yields the first oscillatory cycle local maximum pressure shown on Figure 8.

SIMULATION RESULTS

Simulation free surface profile

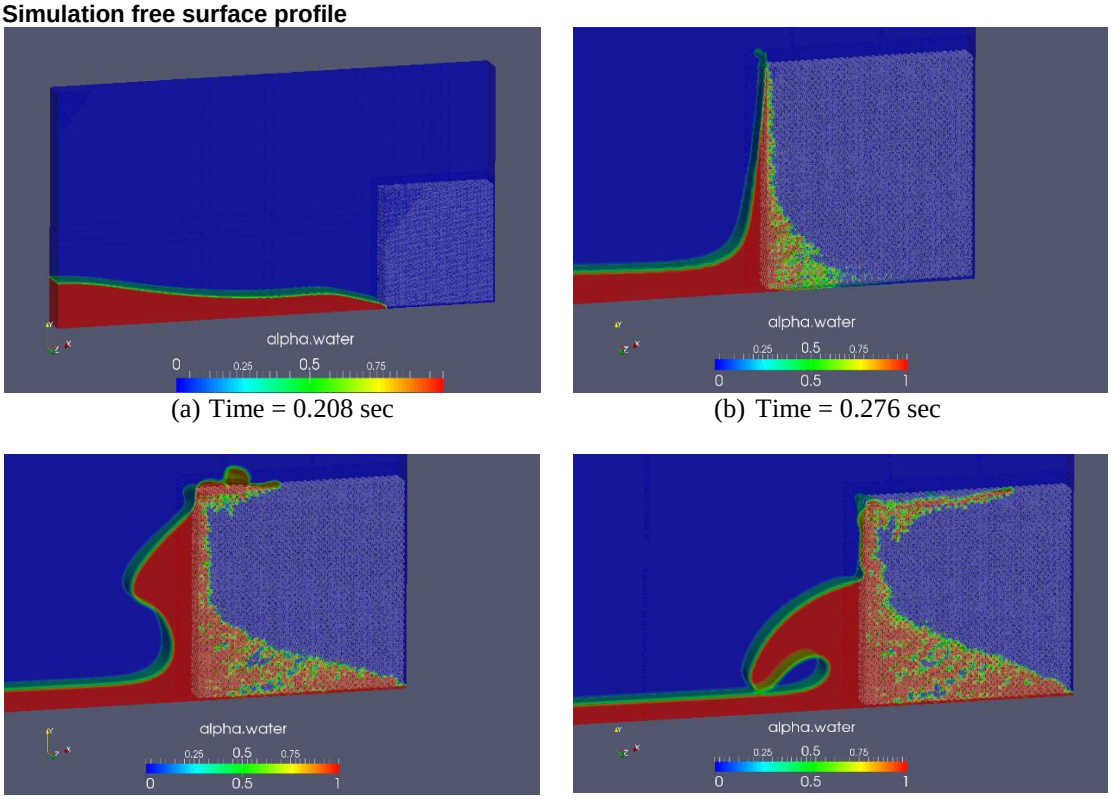

(a) Time = 0.208 sec (b) Time = 0.276 sec

(c) Time = 0.450 sec (d) Time = 0.515 sec

Figure 5: Free surface flow profile section (sphere diameter 3.125mm)

Table 2. Simple cubic packing simulation results

Spheres Diameter	25mm	12.5 mm	6.25 mm	3.125 mm
Outflow flow rate (end time of simulation)	506,960 mm^3/sec	365,680 mm^3/sec	163,450 mm^3/sec	70,100 mm^3/sec
Bubble Oscillation Frequency	298.5 Hz	224Hz	199Hz	174Hz
Bubble Oscillation Amplitude	51	300	557.6	580
Entrained bubble radius (analytic prediction)	10.9 mm	14.6mm	16.4mm	18.8mm
Observed Simulation Bubble Volume	12,284 mm^3	12,190 mm^3	16,423 mm^3	16,396 mm^3
Bubble Surface Area	3,930 mm^2	3,800 mm^2	4,294 mm^2	3,612 mm^2
Bubble (Cylindrical) Length	50 mm	50 mm	50 mm	50 mm
Bubble Sphericity*	0.6551	0.6741	0.7227	0.8642
Equivalent entrained bubble radius (simulation)	14.31	14.27	15.77	12.51

*calculated following Wadell (1935)

Pressure signal analyses

Figure 6 below shows the pressure signal for each of the simulations with the varying component sphere diameter porous structures. Also included on the figure is the pressure signal for a wave impact with a solid wall computed using a similar simulation setup. The solid wall impact results are taken from the analysis of Mayon et al. (2016).

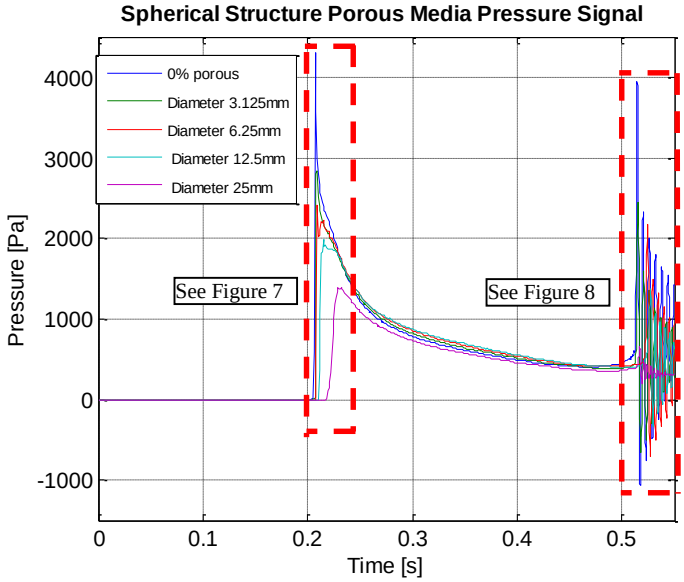

Figure 6: Pressure signals recorded at face of porous structures

Figure 7(a) show the pressure response recorded as the surging flow front impacts the solid and porous walls. There is a slight delay in the impact time for larger spheres as the wave front initially hits the these spheres at a position below P1 (see Figure 4) before flowing vertically up the face of the sphere thereby inducing a pressure increase. The porous structures composed of the larger spheres also exhibit extended impact durations, also termed the rise time, see e.g. (Peregrine, 2003), (Mayon et al., 2016). Whilst the porosity of all the structures is identical the void channels between the larger spheres have a larger surface area opening, this allows the fluid to penetrate these porous structures more easily than the structure with more numerous but smaller surface area openings. This may be explained through the higher wall friction due to the greater specific surface area for the porous assemblages comprising of smaller spheres. The result of this longer rise time is a softer, less impulsive impact for the larger sphere structure. The higher flow rate through the larger sphere porous network supports this assertion.

Figure 7(b) shows the relationship between the sphere diameter and the magnitude of the impulse force. The magnitude of the impulse decreases monotonically as the component sphere diameter increases.

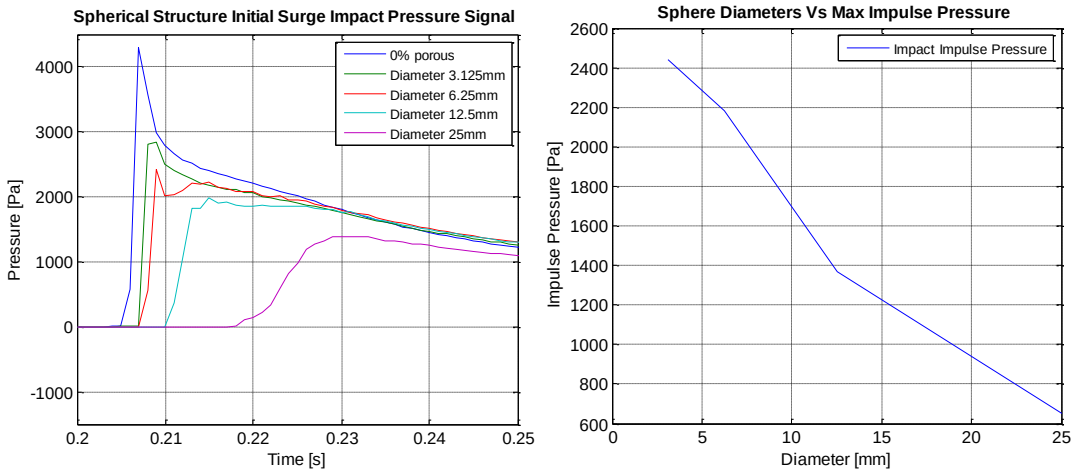

(a) Impact pressure impulse (b) Sphere diameter Vs impact pressure magnitude

Figure 7: Initial impulse impact pressure

Figure 8(a) displays a plot of the pressure signal for the various simulations as the formed vertical jet collapses and converges with the fluid in the bed of the domain. As the jet collapses a plunging breaker is formed as shown in Figure 5(d) and a bubble is entrained which compresses and dilates in a resonant oscillatory manner yielding the cyclic pressure response. As the air entrained within the bubble is compressible, a larger bubble will resonate with a lower frequency as the amount by which it can compress and dilate is dependent upon its volume. The larger bubbles can compress to a greater extent relative to smaller bubbles, thus the amplitude of the oscillatory signal will be greater for these larger bubbles.

The pressure data is converted from the time domain to the frequency domain by preforming a Fourier Transform. Figure 8(b) shows the results of transform and the simulation frequencies and amplitudes are recorded in Table 2. The signal frequencies are plotted against the sphere diameters on Figure 9(a) and the signal amplitudes versus the sphere diameters on Figure 9(b).

The frequency of oscillation increases monotonically as the component sphere diameter increases. Additionally the amplitude of oscillation decreases monotonically. The pressure oscillation frequencies and amplitudes are directly related to the entrained bubble size. Nevertheless, as shown in Table 2 the observed simulation bubble volumes do not follow a trend whereby they increase as the sphere diameter decreases. This may be explained by a number of possibilities. As previously mentioned the smaller sphere based structure allows less fluid to penetrate. Conversely this means that more fluid will be rejected from the face of the porous structure. This in turn will cause to the thicker jet to form. When this jet collapses it falls further away from the wall entraining a larger bubble. This larger bubble will have a lower pressure oscillation frequency and higher amplitude of pressure oscillation. However as shown on Figure 5(c) some of the fluid may collapse on the top of the porous structure and permeate down through the voids.

Another reason the discrepancy in oscillating frequency and amplitude may be due to the bubble shape. Previous researchers have put forward contrasting opinions on the influence of sphericity on the oscillation frequency of a bubble. Strasberg (1953) states that the oscillation frequency of non-spherical bubbles varies only slightly from the oscillation frequency of spherical bubbles, however both Weston (, and Feuillade and Werby (1994) in their studies on non-spherical bubbles (oblate and prolate spheroids) have shown the frequency of oscillation may increase by up to 40% depending on the degree of non-sphericity. Thus for similar volume bubbles their shape may have a large influence on the observed results. Figure 10 shows that there is a large variation in the shape of the bubbles generated in the different simulations. Table 2 records the bubble sphericity for each of the simulations. this is calculated from Equation 16 Wadell (1935):

$$\Psi = \frac{\pi^{\frac{1}{3}}(6V_v)^{\frac{2}{3}}}{A_v} \tag{16}$$

Where V_v and A_v are the volume of the bubble and the surface area of the bubble respectively.

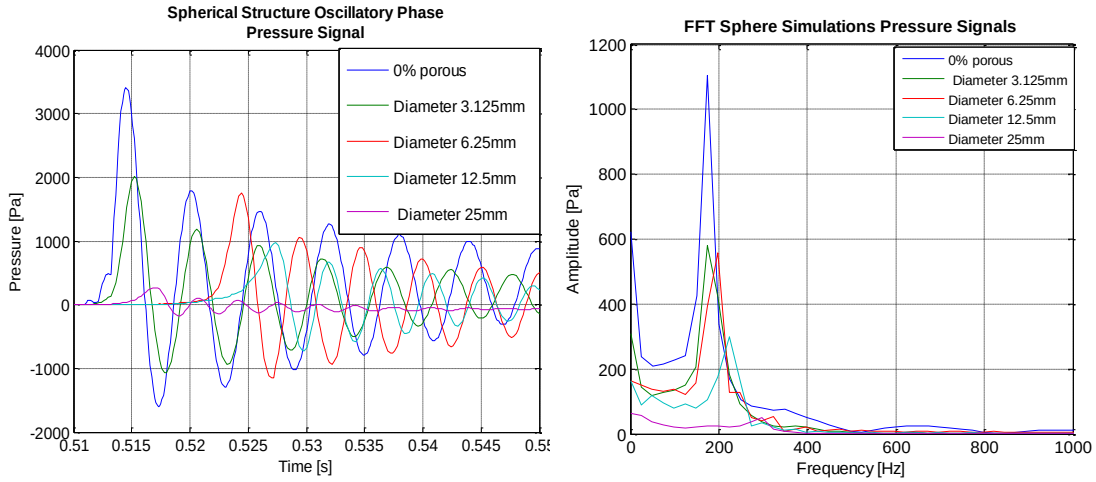

(a) Time domain results (b) Frequency domain results

Figure 8: Simulation oscillatory pressure responses

Finally Figure 11(a-d) shows spatial and temporal pressure signal attenuations within the porous media for each of the porous structures. The oscillatory pressures attenuate more rapidly within the porous structures with the larger component sphere sizes. As the porous structures composed of the smaller component spheres exhibit a lower porosity the fluid trapped within transfers the oscillatory pressures through the porous structure more readily.

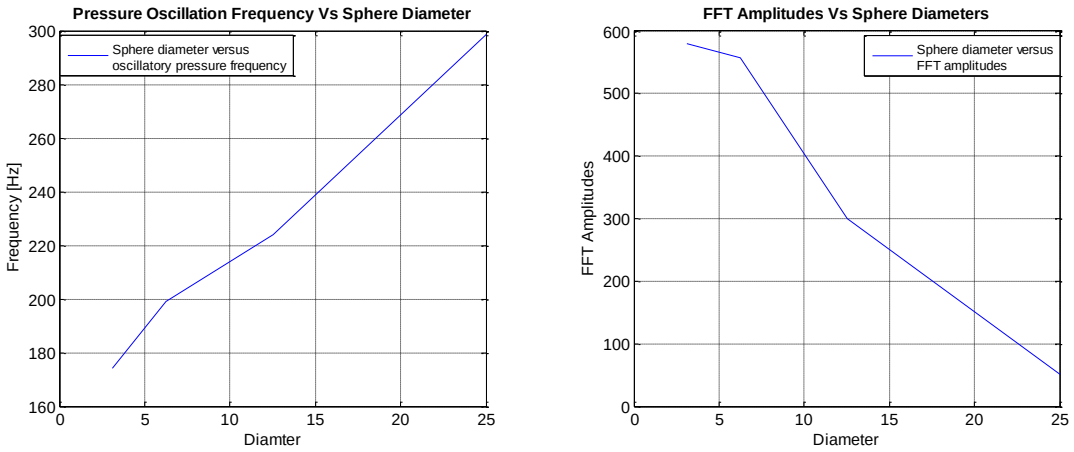

(a) Time domain results (b) Frequency domain results

Figure 9: Sphere diameters Vs FFT results

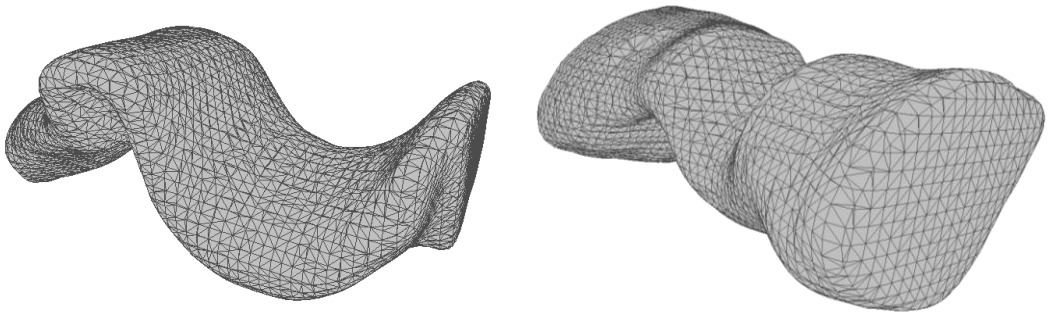

(a) Entrained Bubble geometry from 25mm sphere diameter simulation, t = 0.55 sec

(b) Entrained Bubble geometry from 12.5mm sphere diameter simulation, t = 0.55 sec

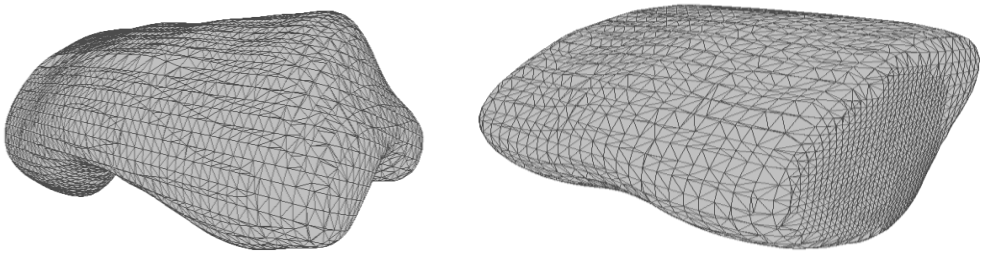

(c) Entrained Bubble geometry from 6.25mm sphere diameter simulation t = 0.55 sec

(d) Entrained Bubble geometry from 3.125mm sphere diameter simulation t = 0.55 sec

Figure 10: Entrained Bubble Geometries

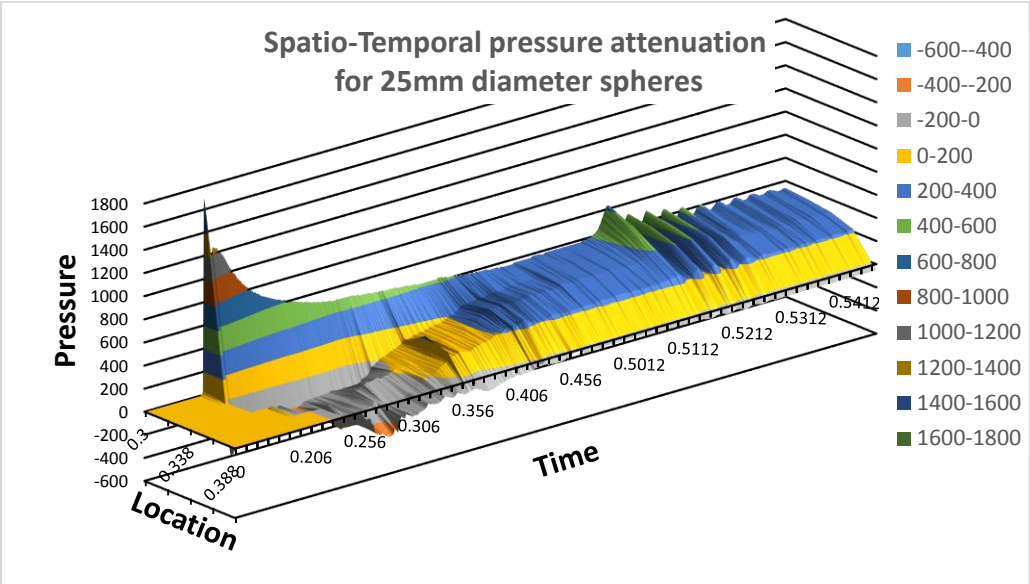

Figure 11(a)

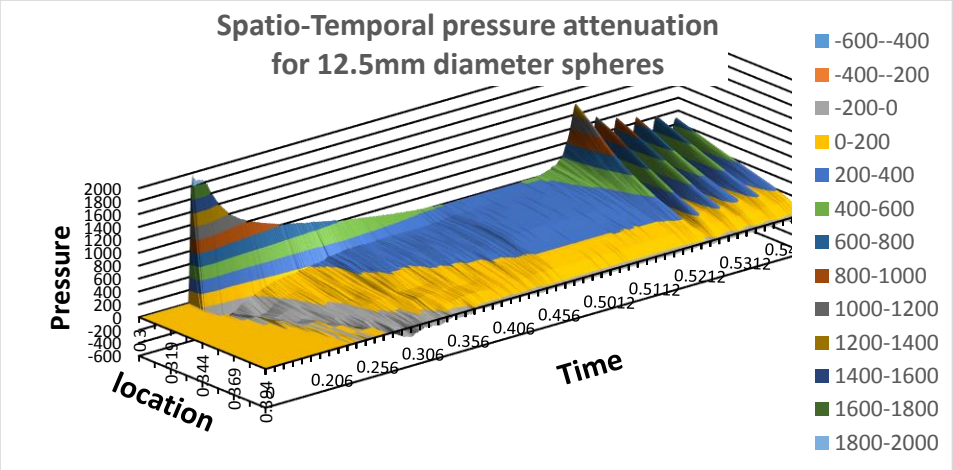

Figure 11(b)

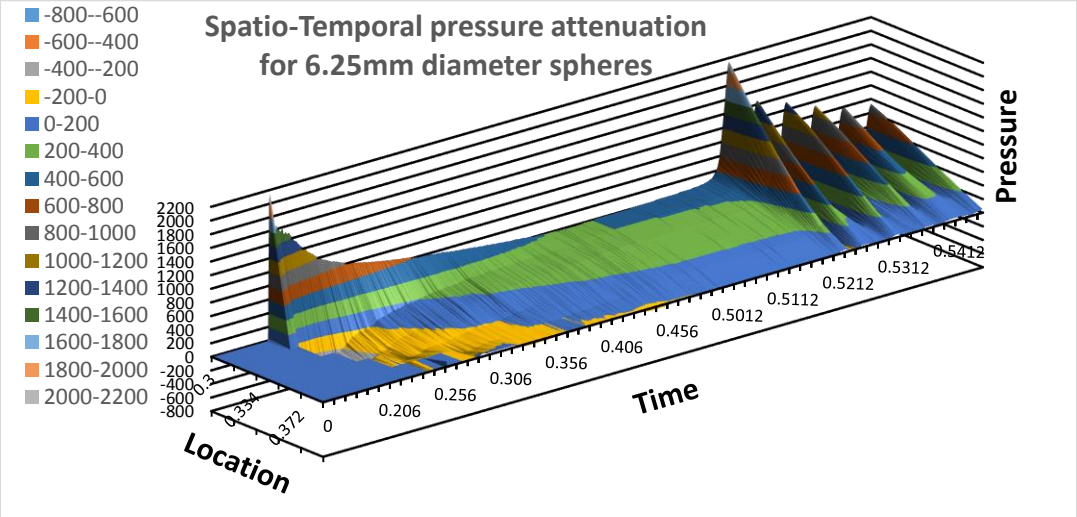

Figure 11(c)

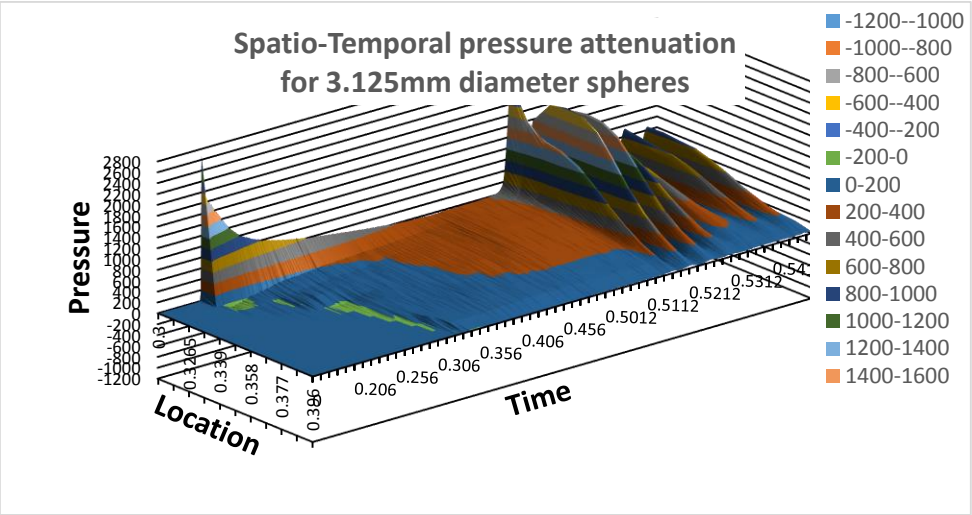

Figure 11(d)

Figure 11: Spatio-temporal pressure attenuation for each porous structure simulation

CONCLUSIONS AND FUTURE DEVELOPMENTS

Wave impact pressures at a range of varying morphology porous structures have been investigated. A thorough parameterisation of the porous media has been presented. The influence of the porous structure on the pressure signal resulting from a surging flow front impact has first been analysed. We clearly show that a porous geometry consisting of larger elemental components reduces the magnitude of the impact pressure impulse but results in a longer pressure rise time. We next investigated the effect of varying porous morphology structures on the pressure signal resulting from a plunging breaker wave impact. Again we demonstrated that a structure with higher specific surface area yielded higher frequency pressure oscillation signals but having a lower magnitude. We also demonstrated that the component sphere size in porous structure influences the shape and volume of the entrained air bubble. The outflow rate (directly related to permeability) has also been shown to be influenced by the specific surface area of the porous geometry. Finally we have shown that the oscillatory pressure signal persists further into the porous structure comprised of the smaller sphere sizes.

Further investigations are in progress to determine the influence of various sphere packing systems and different, more complex, porous morphologies (fibrous, granular etc.) on bubble entrapment during wave impact and the resultant oscillatory pressure signals.

ACKNOWLEDGMENTS

This work is co-funded by the University of Southampton Marine and Maritime Institute (SMMI), the Faculty of Physical Sciences and Engineering (FPSE) and the Faculty of Engineering and the Environment (FEE) under project code 510414106.

REFERENCES

ALAGAN CHELLA, M., BIHS, H. & MYRHAUG, D. 2015. Characteristics and profile asymmetry properties of waves breaking over an impermeable submerged reef. *Coastal Engineering,* 100**,** 26-36.

BAGNOLD, R. A. 1939. INTERIM REPORT ON WAVE-PRESSURE RESEARCH. (INCLUDES PLATES AND PHOTOGRAPHS). *Journal of the Institution of Civil Engineers,* 12**,** 202-226.

BEAR, J. 1988. *Dynamics of fluids in porous media,* New York, Dover.

BERBEROVIĆ, E., VAN HINSBERG, N. P., JAKIRLIĆ, S., ROISMAN, I. V. & TROPEA, C. 2009. Drop impact onto a liquid layer of finite thickness: Dynamics of the cavity evolution. *Physical Review E,* 79**,** 036306.

BREDMOSE, H., PEREGRINE, D. H. & BULLOCK, G. N. 2009. Violent breaking wave impacts. Part 2: Modelling the effect of air. *Journal of Fluid Mechanics,* 641**,** 389-430.

BRUS, G., MIYAWAKI, K., IWAI, H., SAITO, M. & YOSHIDA, H. 2014. Tortuosity of an SOFC anode estimated from saturation currents and a mass transport model in comparison with a real micro-structure. *Solid State Ionics,* 265**,** 13-21.

BULLOCK, G. N., OBHRAI, C., MÜLLER, G., WOLTERS, G., PEREGRINE, D. H. & BREDMOSE, H. Advances in the understanding of wave-impact forces. 2006 / 01 / 01 / 2006. 111-120.

BULLOCK, G. N., OBHRAI, C., PEREGRINE, D. H. & BREDMOSE, H. 2007. Violent breaking wave impacts. Part 1: Results from large-scale regular wave tests on vertical and sloping walls. *Coastal Engineering,* 54**,** 602-617.

CHAN, E. S. & MELVILLE, W. K. 1988. Deep-Water Plunging Wave Pressures on a Vertical Plane Wall. *Proceedings of the Royal Society of London A: Mathematical, Physical and Engineering Sciences,* 417**,** 95-131.

CIVAN, F. 2011. Overview. *Porous Media Transport Phenomena.* John Wiley & Sons, Inc.

DULLIEN, F. A. L. 1992. Introduction. *Porous Media (Second Edition).* San Diego: Academic Press.

FEUILLADE, C. & WERBY, M. F. 1994. Resonances of deformed gas bubbles in liquids. *The Journal of the Acoustical Society of America,* 96**,** 3684-3692.

GHANBARIAN, B., HUNT, A. G., EWING, R. P. & SAHIMI, M. 2013. Tortuosity in Porous Media: A Critical Review. *Soil Science Society of America Journal,* 77**,** 1461-1477.

HATTORI, M., ARAMI, A. & YUI, T. 1994. Wave Impact Pressure on Vertical Walls under Breaking Waves of Various Types. *Coastal Engineering,* 22**,** 79-114.

HIGUERA, P., LARA, J. L. & LOSADA, I. J. 2014. Three-dimensional interaction of waves and porous coastal structures using OpenFOAM®. Part I: Formulation and validation. *Coastal Engineering,* 83**,** 243-258.

HIRT, C. W. & NICHOLS, B. D. 1981. Volume of Fluid (Vof) Method for the Dynamics of Free Boundaries. *Journal of Computational Physics,* 39**,** 201-225.

MARTÍNEZ FERRER, P. J., CAUSON, D. M., QIAN, L., MINGHAM, C. G. & MA, Z. H. 2016. A multi-region coupling scheme for compressible and incompressible flow solvers for two-phase flow in a numerical wave tank. *Computers & Fluids,* 125**,** 116-129.

MAYON, R., SABEUR, Z., TAN, M.-Y. & DJIDJELI, K. 2016. Free surface flow and wave impact at complex solid structures. *12th International Conference on Hydrodynamics.*

MINNAERT, M. 1933. XVI. On musical air-bubbles and the sounds of running water. *The London, Edinburgh, and Dublin Philosophical Magazine and Journal of Science,* 16**,** 235-248.

OUMERACI, H., KLAMMER, P. & PARTENSCKY, H. W. 1993. Classification of Breaking Wave Loads on Vertical Structures. *Journal of Waterway Port Coastal and Ocean Engineering-Asce,* 119**,** 381-397.

PEREGRINE, D. H. 2003. WATER-WAVE IMPACT ON WALLS. *Annual Review of Fluid Mechanics,* 35**,** 23-43.

SABEUR, Z. A., COHEN, J. E., STEPHENS, J. R. & VELDMAN, A. E. P. 1998. Investigation on Free Surface Flow Oscillatory Impact Pressures with the Volume of Fluid Method. *in MJ Baines (ed.), Numerical Methods for Fluid Dynamics* VI**,** pp. 493 - 498.

SABEUR, Z. A., ROBERTS, W. & COOPER, A. J. Development and Use of an Advanced Numerical Model using the VOF Method for the Design of Coastal Structures. *In:* MORTON, K. W. & BAINES, M. J., eds. Numerical Methods for Fluid Dynamics V, 1995. Oxford University Press, 565-573.

STAGONAS, D., MARZEDDU, A., COBOS, F. X. G. I., CONEJO, A. S.-A. & MULLER, G. 2016. Measuring wave impact induced pressures with a pressure mapping system. *Coastal Engineering,* 112**,** 44-56.

STRASBERG, M. 1953. The Pulsation Frequency of Nonspherical Gas Bubbles in Liquids. *The Journal of the Acoustical Society of America,* 25**,** 536-537.

THE OPENFOAM FOUNDATION 2013. The Open Source CFD Toolbox, User Guide & Programmer Guide.

TOPLISS, M. E., COOKER, M. J. & PEREGRINE, D. H. Pressure oscillations during wave impact on vertical walls. 1993 / 01 / 01 / 1993. Publ by ASCE, 1639-1650.

VALLABH, R., BANKS-LEE, P. & SEYAM, A. F. 2010. New Approach for Determining Tortuosity in Fibrous Porous Media. *Journal of Engineered Fibers and Fabrics,* 5**,** 7-15.

WADELL, H. 1935. Volume, Shape, and Roundness of Quartz Particles. *The Journal of Geology,* 43**,** 250-280.

WEMMENHOVE, R., LUPPES, R., VELDMAN, A. E. P. & BUNNIK, T. 2015. Numerical simulation of hydrodynamic wave loading by a compressible two-phase flow method. *Computers & Fluids,* 114**,** 218-231.

WESTON, D. E. 1967. Sound propagation in the presence of bladder fish. Underwater acoustices Vol II, NATO Advanced Study Instute, Copenhagen. edited by V. M. Albers, Plenum, New York, pp. 55-58.